J Exp Biol Advance Online Articles. First posted online on 29 May 2015 as doi:10.1242/jeb.115832
Access the most recent version at http://jeb.biologists.org/lookup/doi/10.1242/jeb.115832

Ontogenetic propulsive transitions by medusae *Sarsia tubulosa*

Kakani Katija,[1*] Sean P. Colin,[2,3] John H. Costello,[3,4] and Houshuo Jiang[1]

[1]*Applied Ocean Physics and Engineering, Woods Hole Oceanographic Institution, Woods Hole, MA 02543, USA*
[2]*Environmental Sciences, Roger Williams University, Bristol, RI 02809, USA*
[3]*Whitman Center, Marine Biological Laboratory, Woods Hole, MA 02543, USA*
[4]*Biology Department, Providence College, Providence, RI 02819, USA*

April 6, 2015

*corresponding author: kakani@mbari.org
Current Address: Monterey Bay Aquarium Research Institute, 7700 Sandholdt Rd, Moss Landing, CA 95039

Acknowledgments

The authors gratefully acknowledge the assistance provided by J.O. Dabiri and E. Klos during field work and animal collections conducted at the Friday Harbor Laboratories (University of Washington) in 2006. We would also like to thank B.J. Gemmell for his assistance with organisms cultured at Marine Biological Laboratories in Woods Hole, MA.

Funding

This work was supported by the National Science Foundation [OCE-1129496 to H.J., OCE-1061353 to J.H.C., and OCE-1242229 to S.P.C.]; and Woods Hole Oceanographic Institution's Office of Research [Ocean Life Institute grant to H.J., Devonshire Foundation grant to K.K.]. K.K. is supported by the Postdoctoral Scholar Program at the Monterey Bay Aquarium Research Institute and the Marine Life Observatory at Hopkins Marine Station (Stanford University).

Author contributions

K.K., H.J., S.P.C., and J.H.C. designed and conceived this study. K.K., S.P.C., and J.H.C. collected the data used in this study. K.K. analysed the data, interpreted the findings, and prepared the manuscript. K.K., H.J., S.P.C., and J.H.C. revised the submission.

Author competing interests

The authors do not have any competing interests.

Disclaimer

The authors are responsible for (1) the accuracy of statements of fact, (2) the authenticity of scientific findings and observations, (3) expressions of scientific or other opinion, and (4) any other material published in the journal.

Abstract

While swimming in their natural environment, marine organisms must successfully forage, escape from predation, and search for mates to reproduce. In the process, planktonic organisms interact with their fluid environment, generating fluid signatures around their body and in their downstream wake through ontogeny. In the early stages of their life cycle, marine organisms operate in environments where viscous effects dominate and govern physical processes. Ontogenetic propulsive transitions in swimming organisms often involve dramatic changes in morphology and swimming behavior. However, for organisms that do not undergo significant changes in morphology, swimming behavior, or propulsive mode, how is their swimming performance affected?

We investigated the ontogenetic propulsive transitions of the hydromedusa *Sarsia tubulosa*, which utilizes jet propulsion and possesses similar bell morphology throughout its life cycle. We used digital particle image velocimetry and high-speed imaging to measure the body kinematics, velocity fields, and wake structures induced by swimming *S. tubulosa* from 1 mm to 10 mm bell exit diameters. Our experimental observations revealed three distinct classes of hydrodynamic wakes: elongated vortex rings for $10 < Re < 30$ (1 to 2 mm bell exit diameter), classical elliptical vortex rings for $Re > 30$ (larger than 2 mm bell exit diameter), and in most instances where $Re > 100$ (larger than 4 or 5 mm bell exit diameter), elliptical vortex rings (or leading vortex rings) were followed by trailing jets. The relative travel distance and propulsive efficiency remained unchanged throughout ontogeny, and the swimming proficiency and hydrodynamic cost of transport decreased nonlinearly.

Key words: jet propulsion, ontogeny, medusan swimming

Introduction

The fitness of marine planktonic organisms depends on their ability to successfully undertake a variety of processes (i.e., forage, search for mates to reproduce, and escape from predation) in their fluid environment (Visser, 2007). While undergoing these activities, organisms generate fluid signatures around their body and in their downstream wake, and the presence of these wakes can directly affect their fitness (Videler et al., 2002; Dickinson, 2003; Visser, 2007). In the early stages of their life cycle, marine organisms operate in environments where viscous effects are significant and govern physical processes (Kiørboe and Visser, 1999; Catton et al., 2012). As organisms grow and develop through ontogeny, individuals experience their fluid environment differently as it transitions from viscous dominated fluid regimes to inertially dominated regimes (Bartol et al., 2008). In order to overcome the changing role of viscosity in their environment, organisms may employ different strategies, biomechanics, and behaviors. Ontogeny studies provide information about these strategies and behaviors as marine organisms interact with their fluid environment.

Swimming organisms utilize many different strategies to travel from one location to the next, which include (but are not limited to) ciliary modes, paddling, and jet propulsion (Vogel, 2008). Ciliary propulsion tends to dominate flows where viscous effects far exceed inertial effects, and Reynolds numbers (*Re*) are up to 10^0 (Childress and Dudley, 2004; Humphries, 2013). Jetting and paddling propulsion are swimming strategies that are more prevalent in intermediary and high Reynolds number regimes (Vogel, 2008, Herschlag and Miller, 2011). Jet propulsion is widespread in biology, and is utilized by many different organisms that include squid (Johnson et al., 1972; Wells and O'Dor, 1991; Anderson and Grosenbaugh, 2005; Bartol et al., 2008), salps (Bone and Trueman, 1983; Madin, 1990; Sutherland and Madin, 2010), and medusae (Daniel, 1983; DeMont and Gosline, 1988; Dabiri et al., 2006). Jet propulsion often involves fast contraction of muscles to create an impulsive jet in the form of a vortex ring (Daniel, 1983; Vogel, 2008). In squid, mantle contraction and expulsion of fluid through a smaller diameter funnel creates strong vortex rings (Johnson et al., 1972; Wells and O'Dor, 1991; Bartol et al., 2008). In medusae, circumferential muscles contract and expel fluid from the subumbrellar cavity to create vortex rings (Daniel, 1983; DeMont and Gosline, 1988; Dabiri et al., 2006).

Free-swimming medusae utilize two conserved swimming modes: rowing and jet propulsion (Colin and Costello, 2002; Costello et al., 2008). For both swimming modes, contraction of the bell by subumbrellar muscles expels fluid from the subumbrellar cavity and creates a starting vortex (Dabiri et al., 2005a). During relaxation of the same subumbrellar muscles, fluid is brought into the subumbrellar cavity due to a drop in internal pressure, and creates a stopping vortex (Dabiri et al., 2005; Sahin et al., 2009). Rowing propulsion is characterized by strong interactions between these stopping and starting vortices to achieve a propulsive advantage (Dabiri et al., 2005). On the other hand, jet propulsion seems to lack this interaction (Weston et al., 2009; Sahin et al., 2009). Based on the medusan morphospace, propulsive mode is largely determined by the fineness ratio, or the ratio between the height and width of the bell (Costello et al., 2008). For medusae with small fineness ratio (oblate body planforms), rowing propulsive mode is observed. For medusae with large fineness ratios (prolate body planforms), jetting propulsive mode is observed (Costello et al., 2008). Interestingly, these swimming modes are strongly linked to behavior with trade-offs for energetics and performance (Ford and Costello, 2000; Costello et al., 2008; Dabiri et al., 2010). Rowing medusae tend to feed and swim constantly, while jetting medusae are often ambush predators, consuming prey that contact tentacles during long, motionless periods (Colin and Costello, 2002; Colin et al., 2003). Since rowing propulsion is more efficient (higher useful work compared with total work) than jetting, and jetting is more proficient (higher peak velocities compared with bell diameter) than rowing, the duration of swimming maximizes feeding rates and minimizes energy expenditure for both rowing and jetting medusae (Colin and Costello, 2002; Colin et al., 2003; Dabiri et al., 2010).

Medusae utilize different strategies to swim and forage through ontogeny (Ford and Costello, 2000; McHenry and Jed, 2003; Weston et al., 2009; Feitl et al., 2009; Blough et al., 2011). Juvenile leptomedusae, *Aequorea victoria* and *Eutonina indicans*, have bells with high fineness ratio (prolate morphology), and after reaching 4 or 5 mm in bell diameter, transition to bells with low fineness ratios (oblate morphology; Weston et al., 2009). Changes in bell morphology were accompanied by changes in swimming mode and behavior: juvenile leptomedusae utilized jet propulsion and rarely swam; adults utilized rowing propulsion and swam continuously (Weston et al., 2009). Studies of jet propulsion in squid through ontogeny also revealed differences in swimming mode and behavior. The propulsive wakes and resulting energetics of *Lolliguncula brevis* (adult squid) and *Doryteuthis pealeii* (squid

paralarvae) showed that squid paralarvae rely almost entirely on jet propulsion for swimming, and adult squid relied on fins more often (Bartol et al., 2008; Bartol et al., 2009a; Bartol et al., 2009b). The propulsive efficiency for squid paralarvae was higher than the adult forms (Bartol et al., 2009a). However, fins were observed to be more active during swimming of adult squid, which may improve propulsive efficiency (Bartol et al., 2008; Bartol et al., 2009a). Therefore, adult squid and squid paralarvae together cannot be used as a model animal for investigating how effective jet propulsion is for an organism that has similar morphology and swimming mode throughout ontogeny.

For organisms going through development in the transitional Reynolds number regime (*Re* from 10^0 to 10^2), it is desirable for them to maintain or keep up with a similar propulsive efficiency and relative travel distance throughout ontogeny (Taylor et al, 2003). This may be due to constraints set by a variety of factors that include (but are not limited to) growth demands, encounter rates, and predator-prey interactions. Organisms have at least two ways to achieve this: by (1) modifying morphology (including propulsive morphology) and swimming mode/behavior, or by (2) maintaining the same morphological features but modifying swimming kinematics. In other words, for organisms that do not undergo significant changes in morphology and propulsive mode through ontogeny, what swimming strategies are employed to overcome relative changes in their fluid environment?

Here we investigate the propulsive transitions over ontogeny of hydromedusa *Sarsia tubulosa* (M. Sars, 1835), which utilizes the same swimming mode (jet propulsion) throughout its life cycle (Colin et al., 2003). In addition, *S. tubulosa* does not undergo significant changes in bell morphology through ontogeny (Edwards, 1978). Therefore, we can investigate swimming kinematics and energetics of *S. tubulosa* to understand how a solely jet-propelled organism is able to overcome the effects of fluid viscosity, and transition to fluid regimes where both inertial and viscous effects are important to fluid processes. For *S. tubulosa*, and many other species of medusae, size is an indicator of developmental stage (Weston et al, 2009; Blough et al, 2011). In this study, we used body size of *S. tubulosa* as a proxy for ontogenetic life stage. We used digital particle image velocimetry and high speed imaging to measure the body kinematics, velocity fields, and wake structures induced by swimming *S. tubulosa* ranging in size from 1 mm to 10 mm bell exit diameters. Using the kinematic data and velocity field data, the propulsive efficiency, swimming proficiency, and

hydrodynamic cost of transport can be evaluated over ontogeny, and a relationship between these quantities and the hydrodynamic wakes generated during swimming can be explored.

Results

Using the methods described below, kinematic and energetic parameters can be quantified to compare swimming ability and biomechanics of *Sarsia tubulosa* across ontogeny. With size scale (specifically bell exit diameter) as a proxy for ontogenetic life stage, scaling laws can be derived for quantities that include maximum swimming speed, distance traveled, swimming proficiency, propulsive efficiency, and hydrodynamic cost of transport, which can elucidate ecomechanical consequences of growth in aquatic biological systems.

Kinematics parameters through ontogeny

As bell exit diameter of *Sarsia tubulosa* increased, the total swimming cycle duration increased linearly (R^2 = 0.84, $p < 0.001$), and the relaxation duration increased at a faster rate than the contraction duration (Fig. 1). The relaxation duration was always longer than the contraction duration over the entire range of bell exit diameter. The coast duration changed with bell exit diameter (R^2 = 0.47, $p < 0.001$), however there are instances where no coasting phase was observed. Differences in bell kinematics and size resulted in differences in swimming speed (Fig. 2). The normalized bell exit diameter (the ratio between time-varying bell exit diameter and maximum bell exit diameter; Fig. 2A) and normalized swimming speed (the ratio between time-varying swimming speed and maximum swimming speed; Fig. 2B) varied with normalized time (time divided by total swimming cycle time). As bell exit diameter increased, the contraction phase duration increased (also shown in Fig. 1). The normalized swimming speed for the 1 mm exit diameter *S. tubulosa* decayed rapidly compared to the larger size classes. For the 9 mm exit diameter *S. tubulosa*, the maximum swimming speed nearly coincided with the end of the contraction phase. For the smaller size classes, the maximum swimming speed was reached approximately 0.09 s prior to the end of the contraction phase, which constituted 23% of the contraction phase duration.

Average values for contraction time (t_c), distance traveled per swimming cycle (d), and maximum swimming speed (U_{max}) are shown for each size class in Table 1. A comparison of all individuals revealed that as bell exit diameter increased, the distance traveled increased linearly (R^2 = 0.80), whereas the maximum swimming speed increased as a power law (R^2 = 0.60; Fig. 3B). However, this increasing trend was reversed when the swimming speed was normalized by animal size (or bell exit diameter, D_e; Fig. 3D). As bell exit diameter increased, the swimming proficiency decreased to the power of -0.63 (R^2 = 0.88). The relative travel distance (travel distance normalized by bell exit diameter; Fig. 3C) had substantial variability with increasing bell exit diameter, and a linear regression (not shown) was found to be not significant (R^2 = 0.04, $p > 0.05$).

Dimensionless parameters, such as Reynolds number *Re* and Strouhal number *St*, provide detail on whether the swimming kinematics of *S. tubulosa* has dynamic similarity across ontogeny. Compiling all collected data revealed a statistically significant linear relationship between bell exit diameter and *Re* (R^2 = 0.96, $p < 0.001$; Fig. 4). The minimum and maximum *Re* is 13 and 300, which corresponded to a 1 mm and 10.5 mm bell exit diameter *S. tubulosa*. This Reynolds number range extended from fluid regimes where viscous forces are significant to intermediary ranges where inertial effects become more important to hydrodynamic processes. Strouhal number remained bounded between 0.1 and 0.3 (Fig. 5; gray dashed lines), with a mean and standard deviation of 0.20 ± 0.07 (Fig. 5; black dashed line) through development. A linear regression of *St* varying with bell exit diameter D_e (not shown) was not statistically significant (R^2 = 0.03, $p > 0.05$).

Hydrodynamic wakes and energetics parameters through ontogeny

Velocity and vorticity fields revealed differences in the hydrodynamic signatures surrounding the body and in the wake of *S. tubulosa* (Fig. 6). Smearing of the vorticity field due to viscosity resulted in an elongated starting vortex structure in the wake of the 1 mm case. For *S. tubulosa* with bell exit diameters of 2 mm and larger, the vortex ring transitioned to a classical elliptical shape. As bell exit diameter increased from 4 mm to 6 mm, the starting vortex structure transitioned from a classical elliptical vortex ring to an elliptical vortex ring with a trailing jet. However, not all *S. tubulosa* with bell exit diameter greater than 5 mm generated a trailing jet, thereby indicating that organisms at this size scale have the ability to exhibit swimming modes with and without a trailing jet. Of the data sets where bell exit

diameter exceeded 4 mm (20 data sets), 15 events where trailing jets emerged in the hydrodynamic wake were measured.

The maximum specific fluid kinetic energy (KE_{max}/ρ) and the maximum specific fluid impulse (I_{max}/ρ) in the propulsive wake of *S. tubulosa* revealed the changing energetics through ontogeny of *S. tubulosa* (Fig. 7). As bell exit diameter increased, KE_{max}/ρ and I_{max}/ρ increased as a power law of 3.23 and 1.89, respectively ($R^2 > 0.90$, $p < 0.001$ for both). Using the values of I_{max}, KE_{max}, and U_{max} (see Table 1 for average values by size class), the propulsive efficiency (η_F, Eqn. 6) across size scales can be determined (Fig. 8). Linear trend lines (not shown) for either formulation of propulsive efficiency were not statistically significant (R^2 values of 0.007 and 0.004 for η_{FD} and η_{FT}, respectively; $p > 0.05$ for both). Finally, the hydrodynamic cost of transport decreased with increasing body exit diameter and body mass (Fig. 9). Power law trend lines for both bell exit diameter and body mass have R^2 values greater than 0.65 and are statistically significant ($p < 0.001$).

Discussion

We observed swimming by *Sarsia tubulosa* through ontogeny starting at 1 mm bell exit diameters through 1 cm. The Reynolds number range experienced through ontogeny (Fig. 4) started at approximately 10 and reached upwards of 300. Throughout ontogeny, *S. tubulosa* were able to achieve jet propulsion and vortex formation during both the contraction and relaxation phases (Fig. 6). However, the characteristics of the wake structures generated by swimming *S. tubulosa* changed through ontogeny. These changes in kinematics and hydrodynamics yielded a reduction in swimming proficiency (i.e. body length s^{-1}) and a non-increasing trend in propulsive efficiency with bell exit diameter. We showed that *S. tubulosa* modifies its swimming kinematics over ontogeny to maintain high propulsive efficiency, which was supported by the narrow Strouhal number range (Fig. 5). This extensive data set is the first to compare the hydrodynamic structures generated by swimming medusae that do not exhibit any substantial changes in morphology or swimming behavior throughout development.

Jetting medusae: experimental vs. numerical models

The smallest size scales of free swimming *S. tubulosa* corresponded to 1 mm bell exit diameters with Reynolds numbers of 10. This size scale was above the apparent lower limit for jet propulsion at $Re = 5$ (Herschlag and Miller, 2011), and the theoretical limit for vortex ring formation (Cantwell, 1986). The total swimming cycle of *S. tubulosa* was comprised of a contraction phase, a coasting period, and then a relaxation phase. The contraction and relaxation durations for the smallest size scales were remarkably similar, with a non-zero coasting phase in between (Fig. 1). As bell exit diameter increased, the total swimming duration increased linearly, and the contraction duration increased more slowly than the relaxation time. The numerical models of Herschlag and Miller (2011) compared the hydrodynamic wakes generated by simulated prolate medusae by maintaining swimming kinematics (where $t_c = 2.43$ s and time of relaxation $t_r = 3\ t_c$) through ontogeny and varying *Re*. The measured contraction phase durations through ontogeny (Fig. 1 and Table 1) were nearly an order of magnitude smaller than those used by Herschlag and Miller (2011). Although true kinematics would significantly improve model results, their observations will nonetheless contribute to our discussion here.

The travel distance over a single swimming cycle increased linearly with increasing bell exit diameter (Fig. 3A). The travel distances reported here were measured after one swimming cycle starting from rest, and the relative travel distance was approximately 2 bell exit diameters through ontogeny (Fig. 3B). After four consecutive swimming cycles, prolate medusae ($Re > 32$) were predicted to travel between five and eight body lengths after starting from rest (Herschlag and Miller, 2011). Despite differences in swimming kinematics and behavior, the observed and predicted relative travel distances are in good agreement. Additionally, the measured maximum swimming speed of *S. tubulosa* began to level off at bell exit diameters larger than 4 or 5 mm (Fig. 3A). The same trend was observed in the prolate model, where for *Re* greater than 100, the average forward velocity began to plateau (Herschlag and Miller, 2011). This power law trend in swimming speed resulted in swimming proficiency decreasing over ontogeny (Fig. 3B) by roughly 60% between 1 mm and 4 or 5 mm bell exit diameters.

Jet propulsion by *S. tubulosa* was observed through ontogeny, with a starting and stopping vortex generated during the contraction and relaxation phases, respectively (Fig. 6).

Our observations differed from Weston et al (2009), where no stopping vortex was observed during the relaxation phase of 2 mm *Aequorea victoria*, a prolate jetting medusae. We suspect that differences in our observations arose from the visualization technique, where the presence of coherent vortex structures relies on the available amount of dye to illuminate the stopping vortex. The generation of a stopping vortex during relaxation was predicted by all numerical and model studies of swimming by prolate adult medusae and through ontogeny (Sahin et al., 2009; Lipinski and Mohseni, 2009; Herschlag and Miller, 2011). Some numerical results suggest that the presence of the velum traps the stopping vortex within the subumbrellar cavity (Lipinski and Mohseni, 2009). The visualization method used in this study did not reveal velum motion for organisms at all size ranges, so we cannot comment on whether the velum retained the stopping vortex. The numerical results of Herschlag and Miller (2011), which did not consider velum kinematics, found that in all *Re* cases, the stopping vortex traveled up into the subumbrellar cavity. We observed that a stopping vortex was generated during bell relaxation, and under its own translational velocity, the stopping vortex remained in the subumbrellar cavity of *S. tubulosa* until it dissipated. As *Re* increased, the presence of the stopping vortex was enhanced and persisted longer than at smaller size scales where viscous diffusion plays a larger role (Herschlag and Miller, 2011).

Our experimental observations revealed three distinct classes of hydrodynamic wakes: elongated vortex rings for $10 < Re < 30$ (1 to 2 mm bell exit diameter), classical elliptical vortex rings for $Re > 30$ (larger than 2 mm bell exit diameter), and in most instances (where $Re > 100$, larger than 4 or 5 mm bell exit diameter), elliptical vortex rings (or leading vortex rings) were followed by trailing jets (Fig. 6). Of the numerical studies considered here, neither study showed hydrodynamic wake structures besides elliptical vortex rings (Sahin et al., 2009; Lipinski and Mohseni, 2009; Herschlag and Miller, 2011). Elongated vortex rings have been observed in wakes created by impulsively jumping copepods and jetting paralarvae (Jiang and Kiørboe, 2011a,b; Bartol et al., 2008; Bartol et al., 2009), whose power stroke (or contraction time) durations are 5 to 100 ms, an order of magnitude less than those prescribed by Herschlag and Miller (2011). In two numerical studies of swimming by adult *S. tubulosa*, realistic kinematics based on experimental data were prescribed (Sahin et al., 2009; Lipinski and Mohseni, 2009), and the formation time of the wake vortex ring was found to be greater than the universal value of 4 (Gharib et al., 1999). It is believed that the time variable change in the velar diameter and the acceleration of fluid from the subumbrellar cavity acted to prevent the emergence of a trailing jet (Mohseni and Gharib, 1998; Sahin et al., 2009), which

is consistent with other observations of formation time by jetting medusae (Dabiri et al., 2006). Although the characterization of vortex formation were not included here, we suspect that the emergence of the trailing jet correspond to hydrodynamic wakes with vortex formation times larger than 8.

Jet propulsion by medusae and squid through ontogeny

The ontogenetic propulsive transitions by juvenile and adult brief squid *Lolliguncula brevis* and *Doryteuthis pealeii* paralarvae (Bartol et al., 2008; Bartol et al., 2009a,b) are similar to those observed in *S. tubulosa.* Squid paralarvae rely heavily on jet propulsion and do not employ their fins until adult life history stages (Bartol et al., 2008; Bartol et al., 2009a,b). Elongated vortex rings formed in the propulsive wakes of *D. pealeii* paralarvae for individuals with dorsal mantle lengths approximately 0.18 cm. As squid grew in size between 3 and 9 cm dorsal mantle lengths, elliptical vortex rings and trailing jets emerged (Bartol et al., 2008; 2009a). For the larger sized *L. brevis*, two jet modes were identified, where jet mode I consisted of a leading vortex and jet mode II consisted of a leading vortex and trailing jet. Interestingly, the authors found that squid less than 5 cm dorsal mantle lengths utilized jet mode I greater than jet mode II (Bartol et al., 2009a). The utilization of jet mode I over jet mode II for smaller size scales are consistent with *S. tubulosa*, where medusae in the Reynolds number range $30 < Re < 100$ would select jet mode I (leading, elliptical vortex ring only), and for $Re > 100$ (4 to 5 mm bell exit diameter), jet modes I and II were employed.

The propulsive efficiency of squid jet propulsion over ontogeny decreased with increasing squid mantle length (Bartol et al., 2008). Paralarvae had significantly higher jet propulsive efficiencies than juveniles or adults, with a measured range of 73.5-95.8% and 49.4-88.8%, respectively (Bartol et al., 2008). As squid grew, fin use increased, and when fin propulsion was considered with the jet, overall propulsive efficiency increased with increasing dorsal mantle length (Bartol et al., 2009a). Therefore, the ontogenetic trend in propulsive efficiency for jetting squid may not be clear since the use of fins may reduce the dependence on jet propulsion for adult squid. Using the same formulation for propulsive efficiency based on the thrust produced in the jet wake (η_{FT}, Fig. 8), we do not see a significant decreasing trend with bell exit diameter in *S. tubulosa*. To be sure, propulsive efficiency (based on the drag produced during swimming, η_{FD}) of jetting medusae utilizing

jet mode II is less than similarly sized rowing medusae generating propulsive wakes similar to jet mode I (Dabiri et al., 2010). If all adult *S. tubulosa* utilized jet mode II, we may see a stronger decreasing trend in propulsive efficiency over ontogeny (Fig. 8).

Interestingly, ontogenetic studies of squid and medusae have shown that they are able to exhibit different swimming modes and generate different hydrodynamic wakes through ontogeny, with selection for some swimming modes in a specific Reynolds number range. In this study, we show that elongated vortex rings were utilized in *S. tubulosa* where $Re < 30$ (1 to 2 mm bell exit diameters), and classical elliptical vortex rings were solely exhibited between $30 > Re > 100$ (2 to 4 mm bell exit diameters). Beyond Reynolds numbers of 100 (> 4 or 5 mm bell exit diameters), adult *S. tubulosa* swim by generating elliptical vortex rings (jet mode I) and leading vortex rings with trailing jets (jet mode II). Instead of transitioning from jet mode I to jet mode II at 4 or 5 mm bell exit diameters, some leptomedusae (*Aequorea victoria* and *Eutonina indicans*) transition to large, oblate, rowing medusae at the same size range (Weston et al., 2009). This transition in morphology and swimming mode was also accompanied by changes in behavior, with *A. victoria* and *E. indicans* swimming nearly continuously as adult rowing medusae. The reasons for this rapid transition between a jetting medusa to a rowing medusa at 4 or 5 mm bell diameters in *A. victoria* and *E. indicans* may be related to this transition between jet mode I and jet mode II, where jet mode II is energetically less efficient (Dabiri et al., 2010).

Hydrodynamic cost of transport over ontogeny

The hydrodynamic cost of transport (*HCOT*), unlike the total cost of transport (*COT*), relies on the quantification of energy invested during jetting to estimate the total energy (including the metabolic investment) expended during locomotion. Although the hydrodynamic cost of transport provides only a minimum estimate of metabolic economy, we expect that the behavior of hydrodynamic cost of transport across ontogeny will reflect the total cost of transport. Metabolic rates for other medusae utilizing rowing propulsion have been collected for *Aurelia aurita*, *Stomolophus meleagris*, and *Stomotoca atra* (Uye and Shimauchi, 2005; Larson, 1987; Daniel 1985). Although respiration rates have been quantified for similarly sized *Gonionemus vertens* (Daniel, 1985), metabolic rates across ontogeny for jet-propelled medusae have yet to be measured. Therefore the use of hydrodynamic cost of transport as a proxy for total cost of transport is warranted.

The *HCOT* for *S. tubulosa* ranged from 0.01 to 10 J kg^{-1} m^{-1} for body masses from 10^{-4} to 1 g (Fig. 9B). Although these values were higher than those reported for *S. meleagris* (Larson 1987), the results here represent size ranges smaller than those reported for *S. meleagris.* For organisms with body mass of 0.01 g, the values of *HCOT* for *S. tubulosa* were consistent with total cost of transport values for *S. atra and G. vertens* (Daniel, 1985). The high rates of acceleration and deceleration during jet propulsion could explain higher values of *HCOT* compared to *S. meleagris*, a rowing-propelled medusa (Daniel, 1985). When plotted on a log-log plot (Fig. 9B), the *HCOT* of *S. tubulosa* became nonlinear for a range of body masses beyond 0.03 and 0.04 g, corresponding to organisms with bell exit diameters of 5 mm (Table 1). The maximum swimming speed over ontogeny for *S. tubulosa* was also nonlinear; after a linear increase for the smallest bell exit diameters, the maximum swimming speed reached a constant (approximately 4 cm s^{-1}) for bell exit diameters larger than 5 mm. Nonlinearity of *COT* (on log-log plots) and maximum swimming speed has been reported for *S. meleagris*, and was attributed to insufficiently powerful muscle mass in larger organisms (Larson, 1987).

In addition to insufficient muscular power, the change in behavior of *HCOT* and swimming speed may be related to differences in hydrodynamic wake structures, where the generation of a leading vortex and trailing jet were observed for *S. tubulosa* with bell exit diameters larger than 5 mm (Fig. 6). In the case of *S. meleagris* and other rowing-propelled

medusae, we do not expect to see a trailing jet for larger size scales (Costello et al., 2008; Dabiri et al., 2010). Therefore, asymptotic behavior of swimming speed in *S. meleagris* may solely be a result of muscle mass limitations. In the case of *S. tubulosa* and other jet-propelled medusae, hydrodynamic costs combined with insufficiently powerful muscle mass limits the body size of jet-propelled medusae (Costello et al., 2008). These ideas may apply to jet-propelled swimmers more generally, where jet propulsion is used as a sole swimming mechanism for smaller organisms, and jet propulsion is used sparingly or in conjunction with other swimming modes or mechanisms in larger swimmers (e.g., medusae and squid; Colin et al., 2003; Bartol et al., 2008).

Materials and Methods

Measurements of swimming *Sarsia tubulosa* (M. Sars, 1835) began in Spring of 2006 and ended in Spring of 2012, and were conducted at the Marine Biological Laboratory (MBL) and Woods Hole Oceanographic Institution (WHOI; Fall of 2010, Spring and Fall of 2011) in Woods Hole, Massachusetts and Friday Harbor Laboratory (FHL; Spring of 2006 and 2012) in Friday Harbor, Washington. The smallest organisms, 1–4 mm bell exit diameters, were acquired as newly budded medusa from cultures of *S. tubulosa* polyps (temperature at 10° C and salinity of 35 psu, density and viscosity corresponds to 1026.95 kg m^{-3} and 1.354×10^{-6} m^2 s^{-1}). Larger medusae, 3–10 mm diameters, were hand collected from the field in both Woods Hole and Friday Harbor. All medusae were maintained in chilled seawater (10° C and 35 psu).

We used body size scale (specifically bell exit diameter) as a proxy for ontogenetic life stage in cultured and collected organisms. The swimming behavior and fluid interactions of all medusae were analyzed using variably sized rectangular glass filming vessels of dimensions that were sufficiently large enough (dimensions much greater than 20 times the medusan diameters) to avoid wall effects. For all measurements, 10 μm glass beads were added to the filming vessel for seeding visualization. The seawater temperature was carefully maintained at 10-12° C throughout the analyses.

In Spring of 2006 (at FHL), data sets were collected where organisms swam through the plane of a 1-mm thick laser sheet produced by a 250 mW, 532 nm continuous laser

(Wicked Lasers, China). The particle motion induced by swimming *S. tubulosa* was recorded at 30 fps (frames per second) onto a digital video tape via a 720 × 480 pixel CCD array (Sony HDR-FDX1, Sony Electronics Inc., USA) resulting in a viewing area 70 cm^2. In Spring of 2012, a high-speed camera (Fastcam SA3, Photron Inc., Japan) and lens (Nikon Inc., Japan) resulted in viewing areas approximately 25 cm^2. Illumination was achieved by cylindrical optics and a 1 W, 671 nm, red laser (LaVision Inc., Germany), creating a 1 mm thick light sheet. Swimming and resulting flow fields were captured at 1000 fps at 1024 × 1024 pixel resolution.

In Woods Hole, animal swimming motions were captured using a high-speed camera (Fastcam SA3, Photron Inc., Japan), a variety of prime lenses (100, 60, 50, and 35 mm; Carl Zeiss Inc., Germany and Nikon Inc., Japan), and extension tubes to yield viewing areas from 1 cm^2 to 16 cm^2. Illumination was provided by a 300 W, 808 nm, near-infrared laser (Firefly, Oxford Lasers, UK), and built-in optics generated a light sheet 0.5 mm thick. In order to resolve high-speed, short duration flows generated by *S. tubulosa*, images were captured at 1000 fps at full, 1024 × 1024 pixel resolution. Data sets where the body (indicated by the laser sheet intersecting the manubrium) and propulsive wake were bisected by the laser sheet within the camera's field of view before, during, and after the swimming cycle were used for subsequent analysis. Of the 133 data sets collected, results from 67 data sets are presented here.

The wet body mass (m) was estimated from the video images, where the tissue thickness (t) at the bell apex and the maximum diameter of the medusa bell (D) was measured prior to the start of contraction. Assuming that the animal is neutrally buoyant in seawater, the body tissues have the same density as seawater (ρ = 1026.95 kg m^{-3}). The medusan body shape was approximated by a hemiellipsoid, with height characterized by thickness t at the apex (and zero thickness at the mid-point) and width characterized by maximum bell diameter D. Therefore, the mass of the medusan body can be estimated by $m = \rho \frac{2}{3} \left(\frac{D}{2}\right)^2 t$.

Raw video images were used to determine *S. tubulosa* kinematics parameters using an in-house Matlab image processing code. From consecutive images, various points were extracted on the body (Fig. 2A; corresponding to body diameter D, bell exit diameter D_e, body height H, velar diameter, and body width at two different points across the bell), the

duration of swimming cycle was quantified (including the duration of the contraction t_c, coasting, and relaxation phases), and the distance traveled during one swimming cycle was measured. The swimming speed of *S. tubulosa* was computed using finite differencing, and data were smoothed using an in-house Matlab processing code (with a Savitzky-Golay filter) to determine maximum swimming speed (U_{max}). The Reynolds number based on maximum swimming speed (*Re*), Strouhal number (*St*), and swimming proficiency (*P*) are

$$Re = \frac{U_{max}\, D_e}{\nu}, \tag{1}$$

$$St = \frac{f\, A}{U_{max}}, \tag{2}$$

$$P = \frac{U_{max}}{D_e}, \tag{3}$$

where *f* is the stroke frequency (inverse of the swimming cycle duration, $1/t_{tot}$), and *A* is the amplitude of the swimming stroke (approximated as half the bell exit diameter, $D_e/2$).

Velocity fields were calculated with DaVis (LaVision Inc., Germany), a digital particle image velocimetry (DPIV; Adrian, 1991; Willert and Gharib, 1991) software package, using a multi-pass algorithm. For the lower resolution images (720 × 480 pixels) collected in Spring of 2006, the initial and final interrogation window sizes are 132 × 132 pixels and 64 × 64 pixels. For higher resolution images (1024 × 1024 pixels), the initial and final interrogation window sizes are 64 × 64 pixels and 32 × 32 pixels, respectively. For both image resolutions, the overlap between interrogation windows was 50%. Velocity field data were exported from DaVis and additional post-processing steps were conducted using an in-house Matlab processing code.

By assuming that the medusan wake is axisymmetric, we can fully characterize fluid dynamics quantities (i.e., kinetic energy and impulse) using planar measurement data (Katija and Dabiri, 2009; Katija et al., 2011). An in-house Matlab code was used to compute the time-varying specific fluid kinetic energy $KE(t)/\rho$ and specific fluid impulse $I(t)/\rho$ in the wake generated by swimming *S. tubulosa*. For an axisymmetric flow, the specific kinetic energy and specific impulse can be found from the velocity field *u* and the resulting vorticity field ω □□□□□□□$\omega = \nabla \times u$),

where r is the distance from the axis of rotation, V is volume in space, S is an arbitrary surface bounded by a closed contour surrounding the non-zero (positive or negative) vorticity field and ΔS corresponds to the velocity field grid mesh spacing (Saffman, 1992). Total time-varying specific kinetic energy and specific impulse is computed by averaging the two values given by the regions S on either side of the rotational axis (Katija and Jiang, 2013). The maximum specific kinetic energy (KE_{max}/ρ) and maximum specific impulse (I_{max}/ρ) are used to calculate the Froude (or propulsive) efficiency based on the induced body drag (η_{FD}) and the thrust produced by the wake jet (η_{FT}), respectively (Daniel, 1983; Bartol et al., 2008). The general definition of propulsive efficiency is

$$\eta_F = \frac{F\,U_{max}}{F\,U_{max} + {KE_{max}}/{t_c}}, \tag{6}$$

where the term F indicates that either the force due to thrust (F_T) or drag (F_D) can be used, and t_c is the contraction time duration. The drag force can be estimated using an empirical coefficient of drag (C_D) for a sphere in fluid regime $2 \leq Re \leq 2\times10^5$ (White, 1974)

$$\frac{KE(t)}{\rho} = \frac{1}{2}\int_V u(t)^2\,dV \approx \pi \sum_S [u(x,r,t)]^2\, r\, \Delta S, \tag{4}$$

$$I(t)/\rho = \pi \iint_S \omega(t)\, r^2\, dS \approx \pi \sum_S \omega(x,r,t)\, r^2\, \Delta S, \tag{5}$$

$$C_D = \frac{24}{Re} + \frac{6}{1+\sqrt{Re}} + 0.4, \tag{7}$$

and the drag force F_D, is found by

$$F_D = \tfrac{1}{2}\rho\, {u_{max}}^2\, C_D. \tag{8}$$

The mean thrust produced by the jet wake (Bartol et al., 2008) is

$$F_T = {I_{max}}/{t_c}. \tag{9}$$

Finally, the cost of transport (COT) is defined to be the amount of energy required to move a unit mass a unit distance (Schmidt-Nielsen, 1972). In the absence of oxygen consumption data to estimate metabolic rates, the hydrodynamic cost of transport ($HCOT$; McHenry and Jed, 2003) can be used as a proxy for COT, where now the energy (E_{swim}) is the product of the distance traveled (d) and the thrust produced by the jet wake (F_T). Using Eqn. 9, the hydrodynamic cost of transport can be defined as

$$HCOT = \frac{E_{swim}}{m\,d} = \frac{{I_{max}}/{t_c}}{m}, \quad (10)$$

where the distance traveled terms (*d*) in the numerator and denominator cancel, and *m* is the wet body mass. Although the hydrodynamic cost of transport is a minimum estimate of the total cost of transport due to the neglect of metabolic energy, it can still provide interesting results on how ontogenetic changes may affect swimming performance in *S. tubulosa*.

List of Symbols and Abbreviations Used

ΔS	Velocity field grid mesh spacing
η_F	Froude or propulsive efficiency
η_{FD}	Froude or propulsive efficiency based on drag
η_{FT}	Froude or propulsive efficiency based on thrust
ρ	Fluid density
ω	Fluid vorticity
C_D	Coefficient of drag
COT	Total cost of transport
d	Distance traveled during a single swimming cycle
D	Bell diameter
D_e	Bell exit diameter
$DPIV$	Digital Particle Image Velocimetry
E_{swim}	Swimming energy
F	Force
F_D	Force due to drag
F_T	Force due to thrust
H	Bell height
$HCOT$	Hydrodynamic cost of transport
I	Fluid impulse
I_{max}	Maximum fluid impulse
KE	Fluid kinetic energy
KE_{max}	Maximum fluid kinetic energy
m	Jellyfish body mass
P	Swimming proficiency
r	Radial distance from the axis of rotation
Re	Reynolds number
S	Arbitrary surface
t	Bell thickness at apex
t_c	Duration of bell contraction
U_{max}	Maximum swimming speed
V	Volume in space

References

Adrian, R. J. (1991). Particle-imaging techniques for experimental fluid mechanics. *Annual review of fluid mechanics*, ***23***(1), 261-304.

Anderson, E. J. and Grosenbaugh, M. A. (2005). Jet flow in steadily swimming adult squid. *Journal of Experimental Biology*, ***208***, 1125-1146.

Bartol, I. K., Krueger, P. S., Thompson, J. T., and Stewart, W. J. (2008). Swimming dynamics and propulsive efficiency of squids throughout ontogeny. *Integrative and Comparative Biology*, ***48***(6), 720-733.

Bartol, I. K., Krueger, P. S., Stewart, W. J., and Thompson, J. T. (2009). Hydrodynamics of pulsed jetting in juvenile and adult brief squid *Lolliguncula brevis*: evidence of multiple jet modes and their implications for propulsive efficiency. *Journal of Experimental Biology*, ***212***(12), 1889-1903.

Bartol, I. K., Krueger, P. S., Stewart, W. J., and Thompson, J. T. (2009). Pulsed jet dynamics of squid hatchlings at intermediate Reynolds numbers. *Journal of Experimental Biology*, ***212***(10), 1506-1518.

Blough, T., Colin, S. P., Costello, J. H., and Marques, A. C. (2011). Ontogenetic changes in the bell morphology and kinematics and swimming behavior of rowing medusae: the special case of the limnomedusa *Liriope tetraphylla*. *The Biological Bulletin*, ***220***(1), 6-14.

Bone, Q., and Trueman, E. R. (1983). Jet propulsion in salps (Tuunicata: Thaliacea). *Journal of Zoology*, ***201***(4), 481-506.

Cantwell, B. J. (1986). Viscous starting jets. *Journal of Fluid Mechanics*, ***173***, 159-189.

Catton, K. B., Webster, D. R., Kawaguchi, S., and Yen, J. (2011). The hydrodynamic disturbances of two species of krill: implications for aggregation structure. *The Journal of experimental biology*, ***214***(11), 1845-1856.

Childress, S. and Dudley, R. (2004). Transition from ciliary to flapping mode in a swimming mollusc: flapping flight as a bifurcation in Re_{ω}. *Journal of Fluid Mechanics*, ***498***, 257-288.

Colin, S. P. and Costello, J. H. (2002). Morphology, swimming performance and propulsive mode of six co-occurring hydromedusae. *Journal of experimental biology*, ***205***(3), 427-437.

Colin, S. P., Costello, J. H., and Klos, E. (2003). In situ swimming and feeding behavior of eight co-occurring hydromedusae. *Marine Ecology Progress Series*, ***253***, 305-309.

Costello, J. H., Colin, S. P., and Dabiri, J. O. (2008). Medusan morphospace: phylogenetic constraints, biomechanical solutions, and ecological consequences. *Invertebrate Biology*, ***127***(3), 265-290.

Dabiri, J. O., Colin, S. P., Costello, J. H., & Gharib, M. (2005). Flow patterns generated by oblate medusan jellyfish: field measurements and laboratory analyses. *The Journal of Experimental Biology*, ***208***(7), 1257-1265.

Dabiri, J. O., Colin, S. P., and Costello, J. H. (2006). Fast-swimming hydromedusae exploit velar kinematics to form an optimal vortex wake. *Journal of Experimental Biology*, ***209***(11), 2025-2033.

Dabiri, J. O., Colin, S. P., Katija, K., and Costello, J. H. (2010). A wake-based correlate of swimming performance and foraging behavior in seven co-occurring jellyfish species. *The Journal of experimental biology*, ***213***(8), 1217-1225.

Daniel, T. L. (1983). Mechanics and energetics of medusan jet propulsion. *Canadian*

Journal of Zoology, ***61***(6), 1406-1420.

Daniel, T. L. (1985). Cost of locomotion: unsteady medusan swimming. *Journal of Experimental Biology*, ***119***(1), 149-164.

DeMont, M. E. and Gosline, J. M. (1988). Mechanics of jet propulsion in the hydromedusan jellyfish, *Polyorchis penicillatus*: II. Energetics of the jet cycle. *Journal of experimental biology*, ***134***(1), 333-345.

Dickinson, M. (2003). Animal locomotion: how to walk on water. *Nature*, ***424***(6949), 621-622.

Edwards, C. (1978). The hydroids and medusae *Sarsia occulta* sp. nov. *Sarsia tubulosa*, 291-311.

Feitl, K. E., Millett, A. F., Colin, S. P., Dabiri, J. O., and Costello, J. H. (2009). Functional morphology and fluid interactions during early development of the scyphomedusa Aurelia aurita. *The Biological Bulletin*, ***217***(3), 283-291.

Ford, M. D. and Costello, J. H. (2000). Kinematic comparison of bell contraction by four species of hydromedusae. *Scientia Marina*, ***64***(S1), 47-53.

Gharib, M., Rambod, E., and Shariff, K. (1998). A universal time scale for vortex ring formation. *Journal of Fluid Mechanics*, ***360***, 121-140.

Herschlag, G. and Miller, L. (2011). Reynolds number limits for jet propulsion: A numerical study of simplified jellyfish. *Journal of theoretical biology*, ***285***(1), 84-95.

Humphries, S. (2013). A physical explanation of the temperature dependence of physiological processes mediated by cilia and flagella. *Proceedings of the National Academy of Sciences*, ***110***(36), 14693-14698.

Jiang, H. and Kiørboe, T. (2011a). The fluid dynamics of swimming by jumping in copepods. *Journal of The Royal Society Interface*, rsif20100481.

Jiang, H. and Kiørboe, T. (2011b). Propulsion efficiency and imposed flow fields of a copepod jump. *The Journal of experimental biology*, ***214***(3), 476-486.

Johnson, W., Soden, P. D., and Trueman, E. R. (1972). A study in jet propulsion: an analysis of the motion of the squid, *Loligo vulgaris*. *Journal of Experimental Biology*, ***56***(1), 155-165.

Katija, K. and Dabiri, J. O. (2009). A viscosity-enhanced mechanism for biogenic ocean mixing. *Nature*, ***460***(7255), 624-626.

Katija, K., Beaulieu, W. T., Regula, C., Colin, S. P., Costello, J. H., and Dabiri, J. O. (2011). Quantification of flows generated by the hydromedusa *Aequorea victoria*: a Lagrangian coherent structure analysis. *Marine Ecology Progress Series*, ***435***, 111-123.

Katija, K. and Jiang, H. (2013). Swimming by medusae *Sarsia tubulosa* in the viscous vortex ring limit. *Limnology and Oceanography: Fluids and Environments*, ***3***, 103-118.

Kiørboe, T. and Visser, A. (1999). Predator and prey perception in copepods due to hydromechanical signals. *Marine Ecology-Progress Series*, ***179***, 81-95.

Larson, R. J. (1987). Costs of transport for the scyphomedusa Stomolophus meleagris L. Agassiz. *Canadian journal of zoology*, ***65***(11), 2690-2695.

Lipinski, D. and Mohseni, K. (2009). Flow structures and fluid transport for the hydromedusae *Sarsia tubulosa* and *Aequorea victoria*. *The Journal of experimental biology*, ***212***(15), 2436-2447.

Madin, L. P. (1990). Aspects of jet propulsion in salps. *Canadian Journal of Zoology*, ***68***(4), 765-777.

McHenry, M. J., and Jed, J. (2003). The ontogenetic scaling of hydrodynamics and swimming performance in jellyfish (*Aurelia aurita*). *Journal of Experimental Biology*, ***206***(22), 4125-4137.

Mohseni, K. and Gharib, M. (1998). A model for universal time scale of vortex ring

formation. *Physics of Fluids (1994-present)*, ***10***(10), 2436-2438.

Wells, M. J. and O'Dor, R. K. (1991). Jet propulsion and the evolution of the cephalopods. *Bulletin of marine science*, ***49***(1-2), 419-432.

Saffman, P. G. (1992). *Vortex dynamics*. Cambridge university press.

Sahin, M., Mohseni, K., and Colin, S. P. (2009). The numerical comparison of flow patterns and propulsive performances for the hydromedusae *Sarsia tubulosa* and *Aequorea victoria*. *Journal of Experimental Biology*, ***212***(16), 2656-2667.

Schmidt-Nielsen, K. (1972). Locomotion: energy cost of swimming, flying, and running. *Science*, ***177***(4045), 222-228.

Sutherland, K. R. and Madin, L. P. (2010). Comparative jet wake structure and swimming performance of salps. *The Journal of experimental biology*, ***213***(17), 2967-2975.

Uye, S. I. and Shimauchi, H. (2005). Population biomass, feeding, respiration and growth rates, and carbon budget of the scyphomedusa *Aurelia aurita* in the Inland Sea of Japan. *Journal of Plankton Research*, ***27***(3), 237-248.

Videler, J. J., Stamhuis, E. J., Müller, U. K., and van Duren, L. A. (2002). The scaling and structure of aquatic animal wakes. *Integrative and comparative biology*, ***42***(5), 988-996.

Vogel, S. (2008). Modes and scaling in aquatic locomotion. *Integrative and comparative biology*, ***48***(6), 702-712.

Visser, A. W. (2007). Motility of zooplankton: fitness, foraging and predation. *Journal of Plankton research*, ***29***(5), 447-461.

Weston, J., Colin, S., Costello, J. H., and Abbott, E. (2009). Changing form and function during development in rowing hydromedusae. *Marine Ecology Progress Series*, **374**, 127-134.

White, F. M. (1979). Viscous fluid flow, 1974.

Willert, C. E. and Gharib, M. (1991). Digital particle image velocimetry. *Experiments in fluids*, ***10***(4), 181-193.

Tables

Table 1. Results from 49 data sets of swimming by *Sarsia tubulosa* across ten different size classes. The size classes are based on bell exit diameter (D_e), where N indicates the number of individuals per size class. The data include average values (± standard deviation) of the body mass (m), time of contraction (t_c), distance traveled per swimming cycle (d), maximum swimming speed (U_{max}), maximum specific fluid kinetic energy (KE_{max}/ρ), maximum specific fluid impulse (I_{max}/ρ), Reynolds number based on U_{max} (Re), swimming proficiency (P), propulsive efficiency based on the body drag (η_{FD}), propulsive efficiency based on the wake thrust (η_{FT}), and the hydrodynamic cost of transport ($HCOT$).

D_e [mm]	N [ ]	m [g]	t_c [s]	d [mm]	U_{max} [cm s^{-1}]	KE_{max}/ρ [m^5 s^{-2}]	I_{max}/ρ [m^4 s^{-1}]	Re [ ]	P [s^{-1}]	η_{FD} [%]	η_{FT} [%]	$HCOT$ [J kg^{-1} m^{-1}]
1	8	$4.32 \times 10^{-4} \pm 2.47 \times 10^{-4}$	0.06 ± 0.01	2.93 ± 0.46	2.10 ± 0.40	$7.52 \times 10^{-13} \pm 5.12 \times 10^{-13}$	$9.23 \times 10^{-11} \pm 1.41 \times 10^{-11}$	19.15 ± 6.23	17.61 ± 3.52	85.81 ± 8.86	74.16 ± 11.97	4.18 ± 1.32
2	11	$4.05 \times 10^{-3} \pm 2.28 \times 10^{-3}$	0.10 ± 0.02	4.64 ± 1.72	2.73 ± 0.49	$1.30 \times 10^{-11} \pm 1.08 \times 10^{-11}$	$7.06 \times 10^{-10} \pm 4.22 \times 10^{-10}$	51.17 ± 12.96	11.05 ± 2.22	79.83 ± 9.81	62.62 ± 10.59	1.88 ± 0.75
3	10	$9.07 \times 10^{-3} \pm 3.15 \times 10^{-3}$	0.11 ± 0.02	6.80 ± 2.63	2.86 ± 0.52	$2.41 \times 10^{-11} \pm 1.27 \times 10^{-11}$	$1.32 \times 10^{-9} \pm 5.02 \times 10^{-10}$	74.75 ± 19.92	8.21 ± 1.19	75.61 ± 7.67	62.07 ± 5.67	1.56 ± 0.72
4	6	$1.31 \times 10^{-2} \pm 2.06 \times 10^{-3}$	0.11 ± 0.02	8.52 ± 2.34	2.94 ± 0.54	$3.06 \times 10^{-11} \pm 1.63 \times 10^{-11}$	$1.62 \times 10^{-9} \pm 6.38 \times 10^{-10}$	94.35 ± 20.02	6.80 ± 1.20	73.69 ± 13.31	62.21 ± 8.29	1.20 ± 0.56
5	3	$2.38 \times 10^{-2} \pm 2.13 \times 10^{-3}$	0.15 ± 0.03	11.66 ± 5.51	3.95 ± 0.19	$8.80 \times 10^{-11} \pm 4.85 \times 10^{-11}$	$5.04 \times 10^{-9} \pm 2.08 \times 10^{-9}$	151.10 ± 4.10	7.67 ± 0.59	81.49 ± 10.58	70.68 ± 6.69	1.54 ± 0.69
6	2	$1.35 \times 10^{-1} \pm 1.51 \times 10^{-4}$	0.20 ± 0.04	12.89 ± 2.78	3.66 ± 0.54	$1.90 \times 10^{-10} \pm 5.54 \times 10^{-11}$	$1.32 \times 10^{-8} \pm 5.29 \times 10^{-9}$	174.30 ± 30.90	5.70 ± 0.66	87.22 ± 7.90	69.72 ± 17.26	0.48 ± 0.10
7	1	1.25×10^{-1}	0.13	14.17	3.12	3.20×10^{-10}	1.34×10^{-8}	171.14	4.22	68.80	56.55	0.83
8	4	$1.66 \times 10^{-1} \pm 1.13 \times 10^{-2}$	0.17 ± 0.04	16.42 ± 4.28	4.07 ± 0.26	$3.42 \times 10^{-10} \pm 1.77 \times 10^{-10}$	$1.37 \times 10^{-8} \pm 4.00 \times 10^{-9}$	259.79 ± 21.17	4.74 ± 0.36	81.61 ± 9.36	63.13 ± 10.98	0.56 ± 0.28
9	2	$1.43 \times 10^{-1} \pm 5.24 \times 10^{-2}$	0.14 ± 0.04	14.68 ± 2.67	3.40 ± 0.69	$2.80 \times 10^{-10} \pm 9.79 \times 10^{-11}$	$1.30 \times 10^{-8} \pm 4.98 \times 10^{-9}$	230.51 ± 45.25	3.71 ± 0.78	72.17 ± 21.10	60.65 ± 4.00	0.70 ± 0.41
10	2	$2.81 \times 10^{-1} \pm 3.81 \times 10^{-2}$	0.22 ± 0.02	20.79 ± 0.29	3.93 ± 0.01	$3.15 \times 10^{-10} \pm 3.97 \times 10^{-11}$	$2.44 \times 10^{-8} \pm 4.27 \times 10^{-9}$	292.26 ± 11.22	3.92 ± 0.14	86.99 ± 3.85	74.98 ± 5.68	0.41 ± 0.03

Figures

Figure 1. Duration of contraction, coast, relaxation, and total swimming cycle with increasing size. (A) Duration of total swimming cycle t_{tot} and (B) contraction t_c (blue, open circles), coast (green, filled circles), and relaxation (red, filled squares) phases through development of *Sarsia tubulosa.* Linear regression curves for contraction (blue line), coast (green line), relaxation (red line), and total swimming cycle (black line) duration have R^2 values corresponding to 0.64, 0.50, 0.64, and 0.84, respectively. All regressions are statistically significant and have a *p*-value less than 0.001.

Figure 2. Kinematics of normalized bell exit diameter and swimming speed of *Sarsia tubulosa* with increasing size. (A) Normalized bell exit diameter kinematics and (B) normalized swimming speed of representative *S. tubulosa* for three different size classes. The bell exit diameter and swimming speed have been normalized by maximum bell exit diameter D_e and maximum swimming speed U_{max} corresponding to the data set. Time has been normalized for each data set by the duration of the total swimming cycle. Dashed blue, green, and red lines indicate the normalized time of minimum bell exit diameter (or normalized time of maximal contraction) for the 1, 4, and 9 mm bell exit diameter cases. The representative data sets for the 1 (blue line), 4 (green line), and 9 mm (red line) bell exit diameter size classes correspond to 111129_sarsia_20, 110729_sarsia_17, and 120613_9p5mm_4b, respectively.

Figure 3. Swimming kinematics parameters of *Sarsia tubulosa* with increasing size scale. (A) Travel distance during a single swimming cycle, d (B) maximum swimming speed, U_{max} (C) relative travel distance, d/D_e and (D) swimming proficiency, $P=U_{max}/D_e$ with increasing bell exit diameter, D_e. Linear and power law regression curves for travel distance, maximum swimming speed, and proficiency have R^2 values corresponding to 0.80, 0.62, and 0.87, respectively; all regressions are statistically significant with a *p*-value less than 0.001. A linear regression curve for relative travel distance (not shown) is not statistically significant ($p > 0.001$).

Figure 4. Reynolds number (*Re*) of *S. tubulosa* based on maximum swimming speed (U_{max}) with bell exit diameter, (D_e). The linear regression curve for *Re* has an R^2 value of 0.96 and *p*-value less than 0.001.

Figure 5. Strouhal number (*St*) of *S. tubulosa* based on swimming frequency $f=1/t_{tot}$, amplitude $A\sim D_e/2$ and maximum swimming speed U_{max}. A linear regression curve for Strouhal number (not shown) is not statistically significant ($p > 0.001$).

Figure 6. Velocity (black vectors) and vorticity (red and blue filled contours) fields of representative *S. tubulosa* for three different size classes. Top panel, 1 mm bell exit diameter; middle panel, 4 mm; bottom panel, 6 mm. For each size class, images (from left to right) correspond to the start of bell contraction, halfway through contraction phase, end of contraction (or start of bell relaxation), halfway through relaxation, and end of relaxation phase. The three panels illustrate the three observed types of jet propulsion (i.e., elongated vortex ring, elliptical vortex ring, and elliptical vortex ring with a trailing jet), where the trailing jet can be clearly identified in the lower panel at time t = 0.203 s. The representative data sets for the 1, 4, and 6 mm bell exit diameter size classes correspond to 101121_sarsia_3, 110729_sarsia_17, and

120613_6p5mm_2, respectively.

Figure 7. Maximum specific fluid kinetic energy and maximum specific fluid impulse with bell exit diameter of *Sarsia tubulosa.* (A) Maximum specific fluid kinetic energy (KE_{max}/ρ) with bell exit diameter, D_e of *S. tubulosa* over ontogeny. (B) Maximum specific fluid impulse (I_{max}/ρ) with bell exit diameter. Power law regression curves for maximum specific fluid kinetic energy and maximum specific fluid impulse are statistically significant ($p < 0.001$) and have R^2 values corresponding to 0.76 and 0.90, respectively.

Figure 8. Froude or swimming efficiency (η_F) of *S. tubulosa* based on the body drag (η_{FD}, black open circles) and wake thrust (η_{FT}, gray filled circles) with bell exit diameter, *D*. Linear regression curves for η_{FD} and η_{FT} (not shown) are not statistically significant ($p > 0.001$) and have R^2 values of 0.007 and 0.004, respectively.

Figure 9. Hydrodynamic cost of transport (*HCOT*) with increasing size of *Sarsia tubulosa.* *HCOT* as a function of (A) bell exit diameter, D_e and (B) body mass, *m.* Power law regression curves are statistically significant ($p < 0.001$) and have R^2 values corresponding to 0.67 and 0.74 in (A) and (B), respectively.

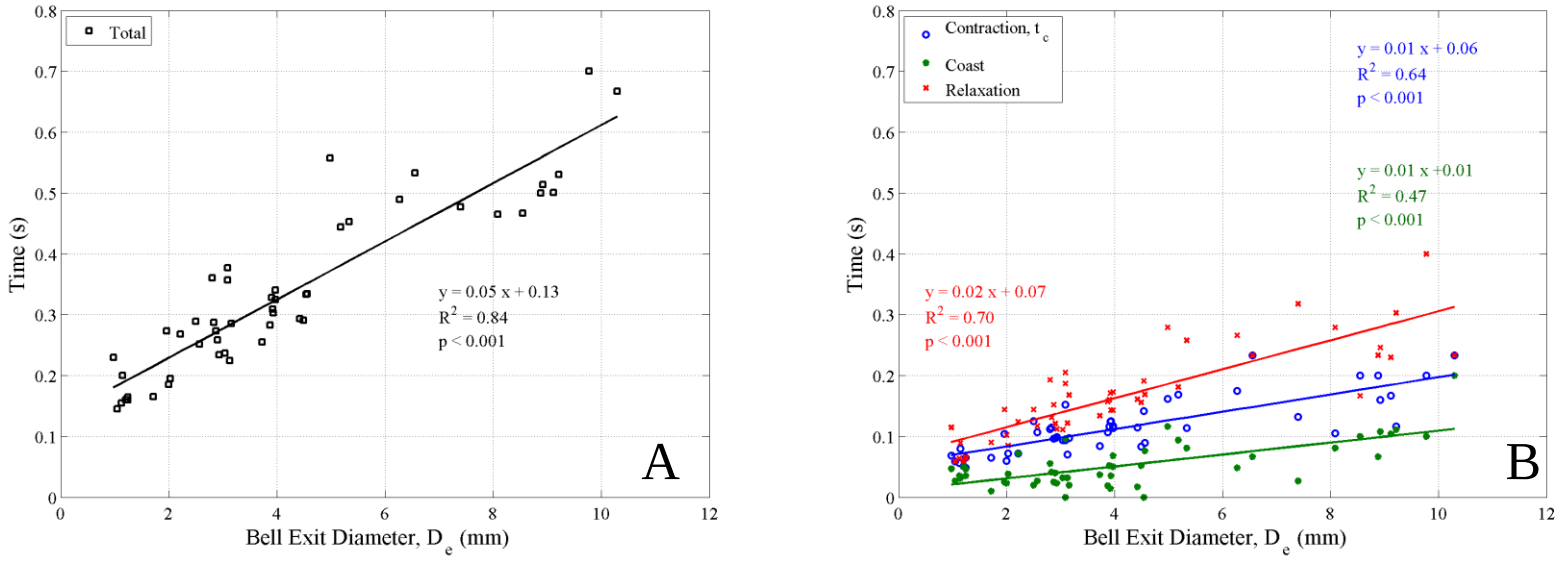

Figure 1

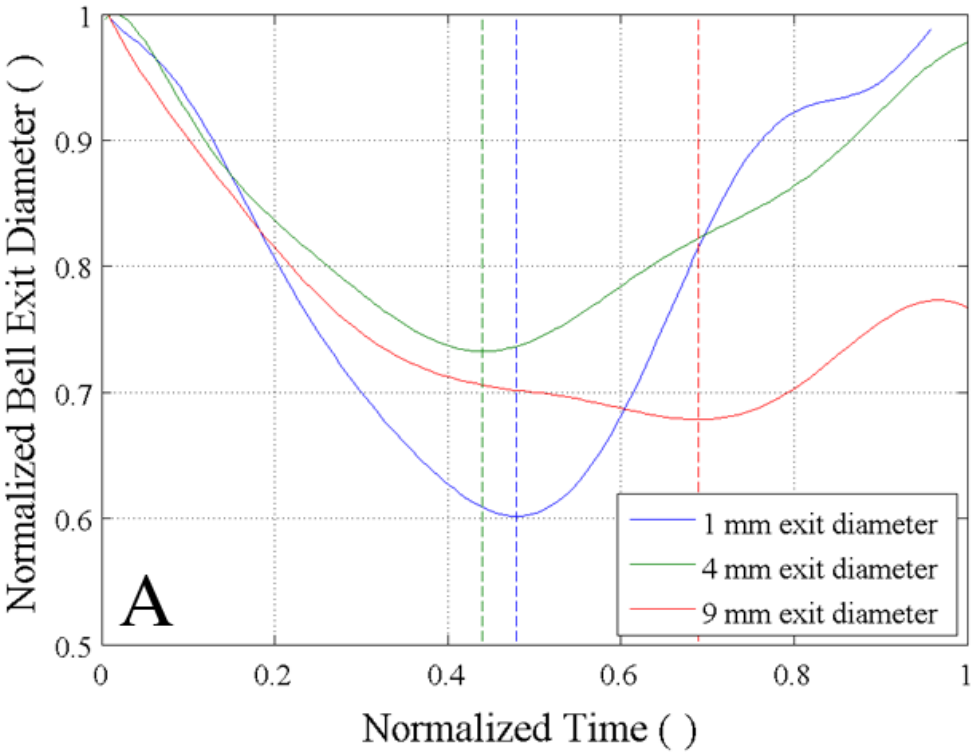

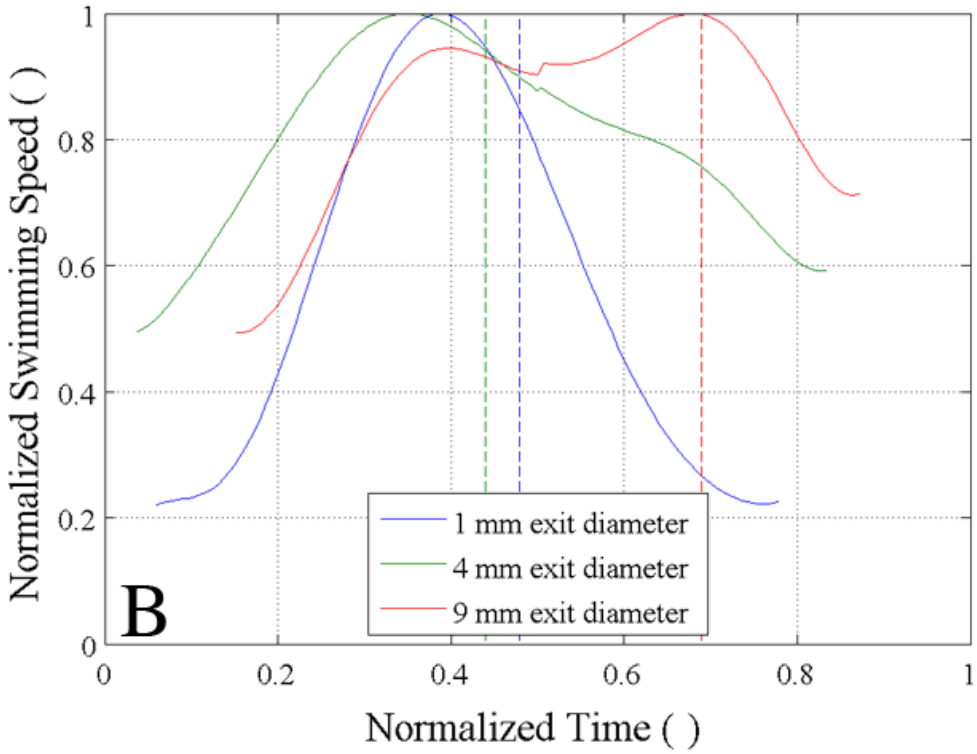

Figure 2

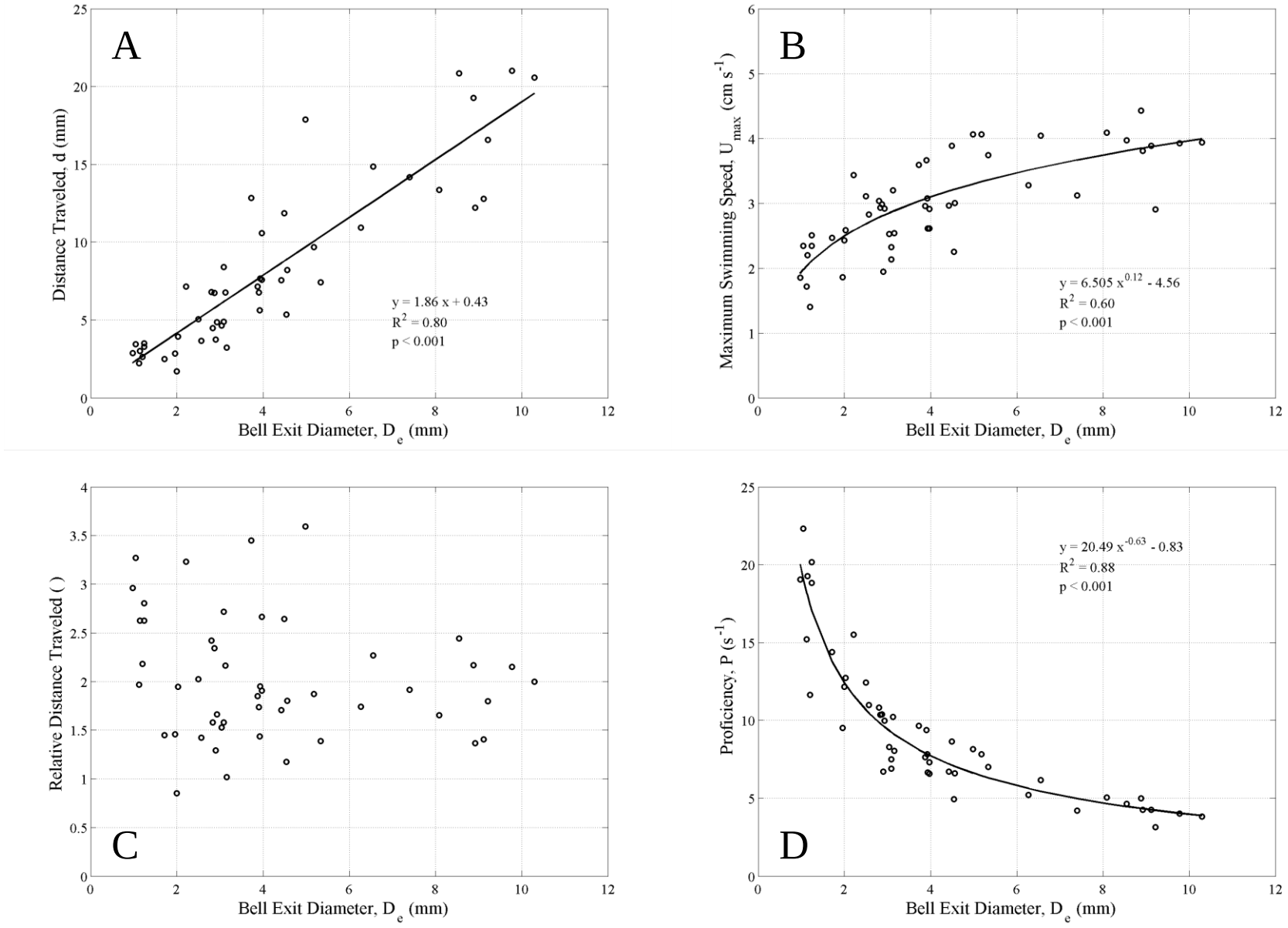

Figure 3

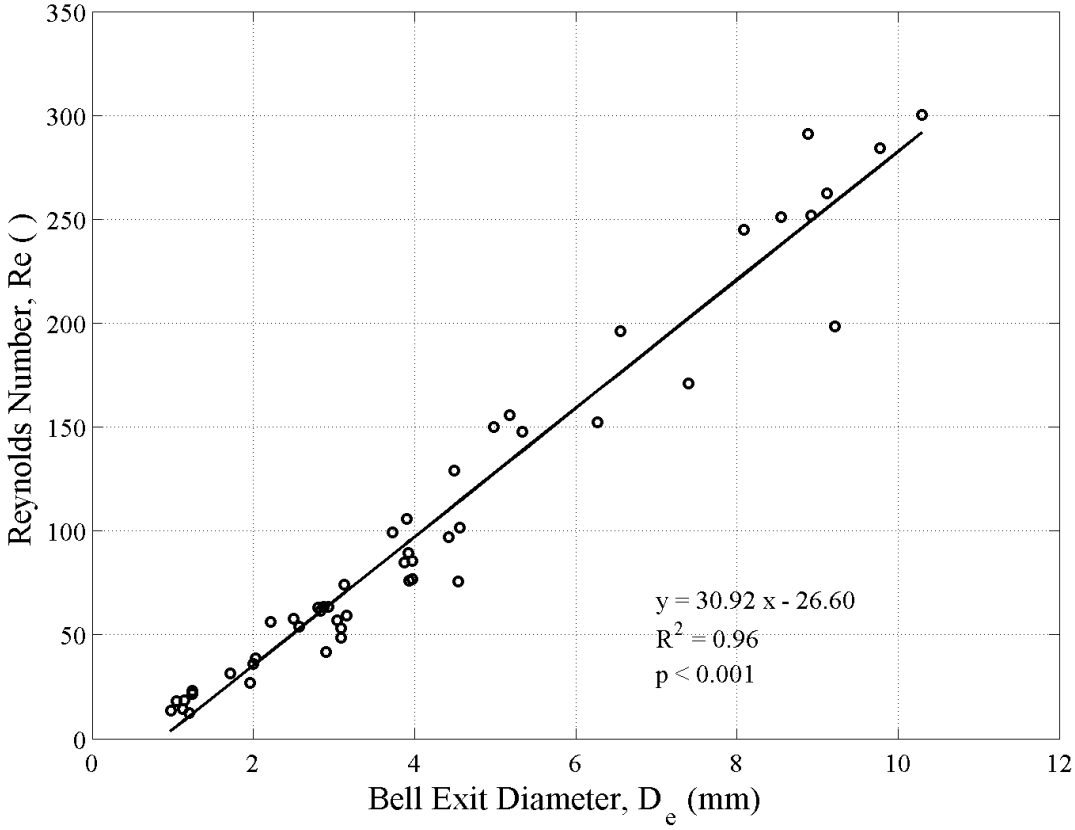

Figure 4

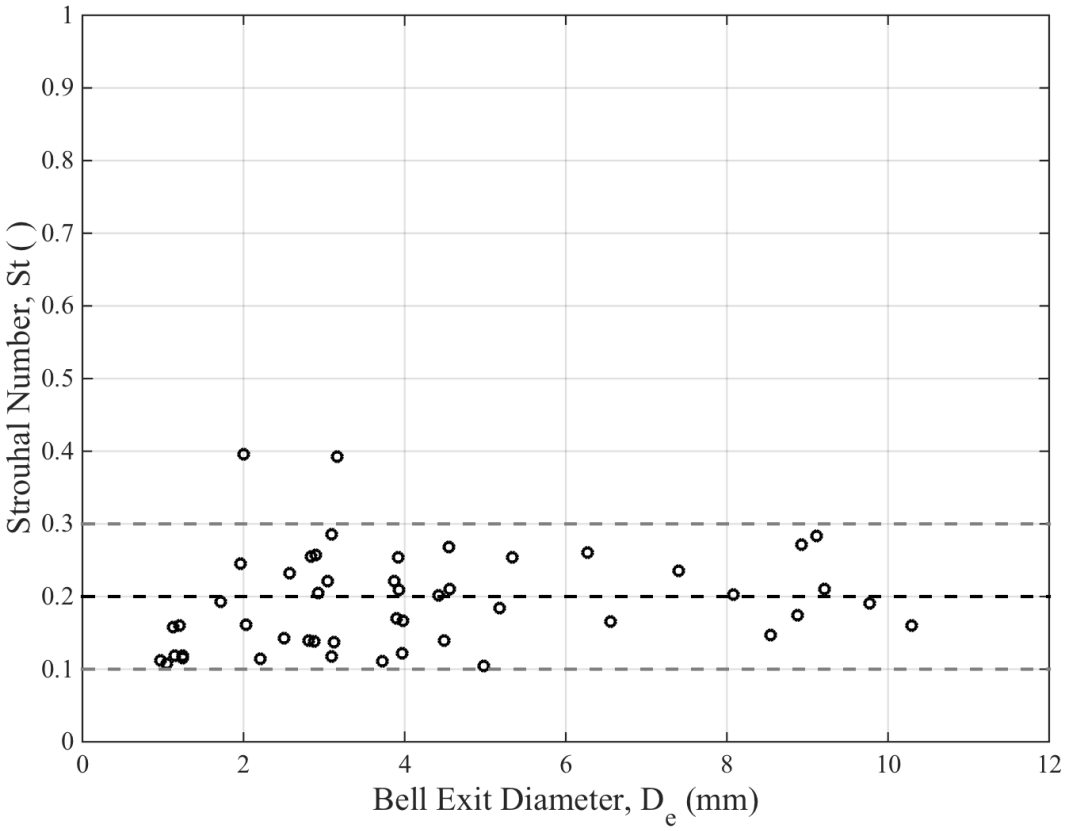

Figure 5

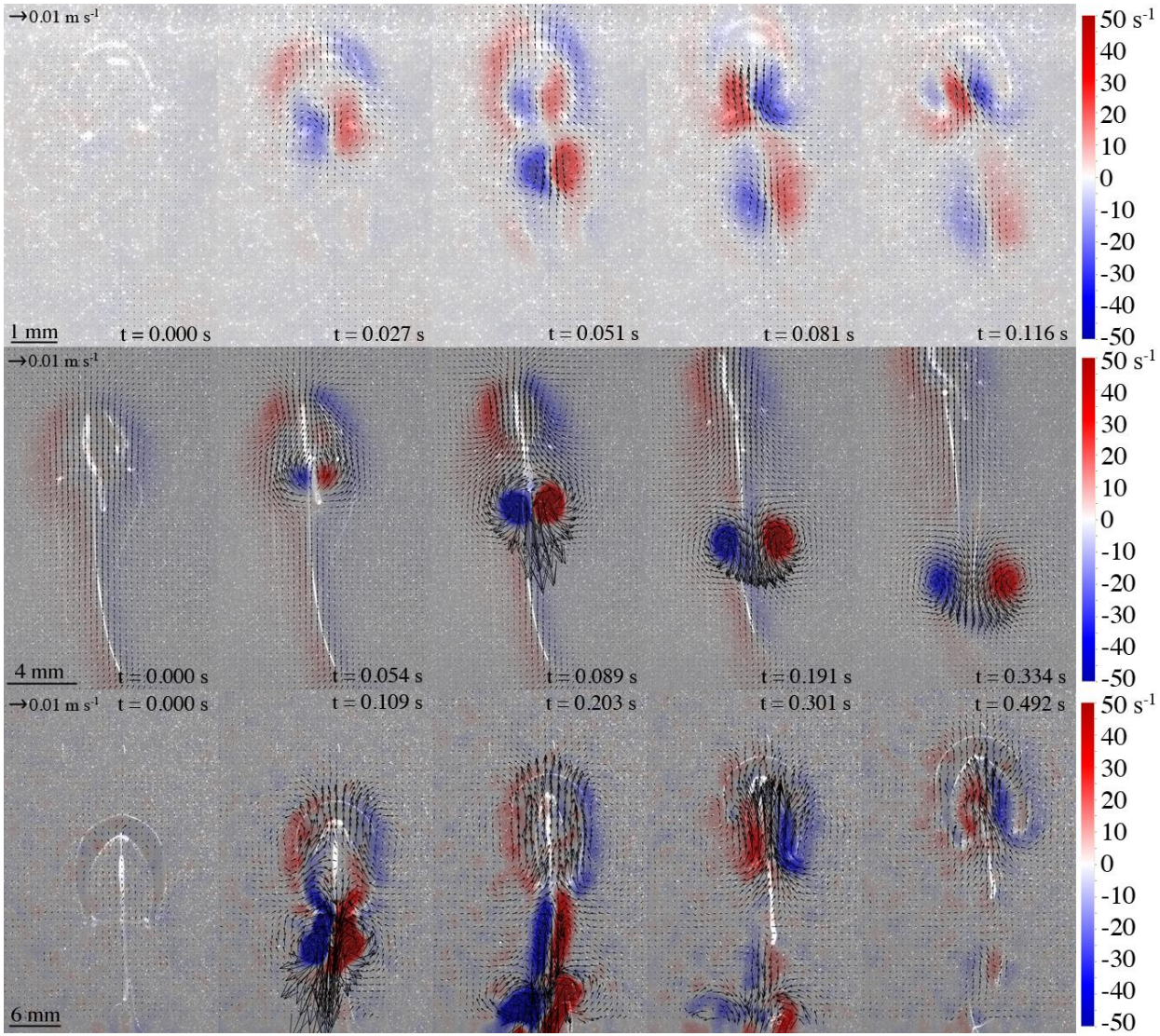

Figure 6

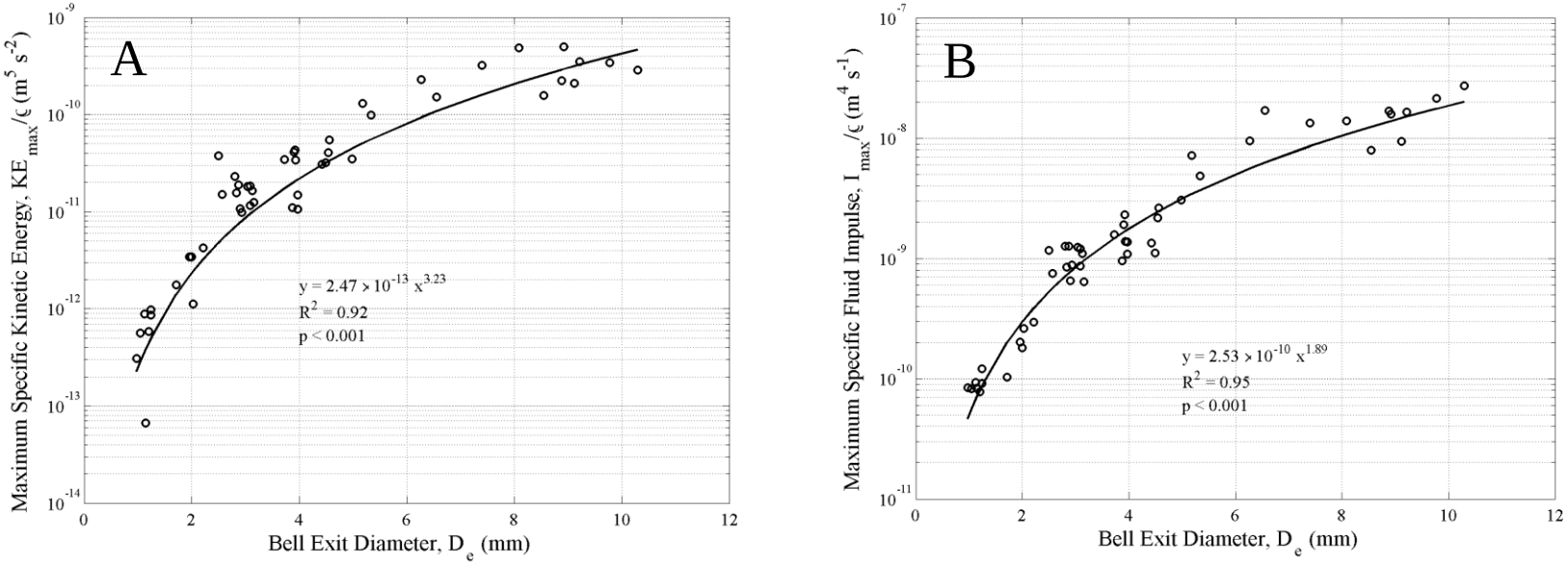

Figure 7

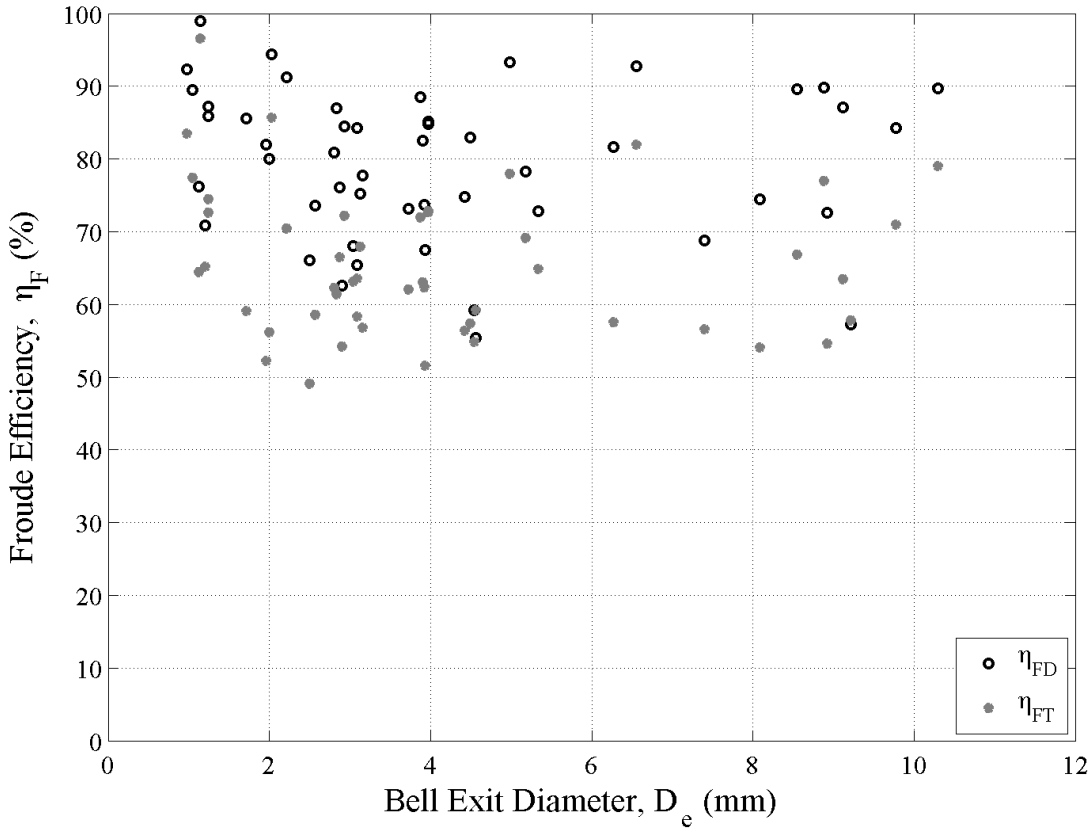

Figure 8

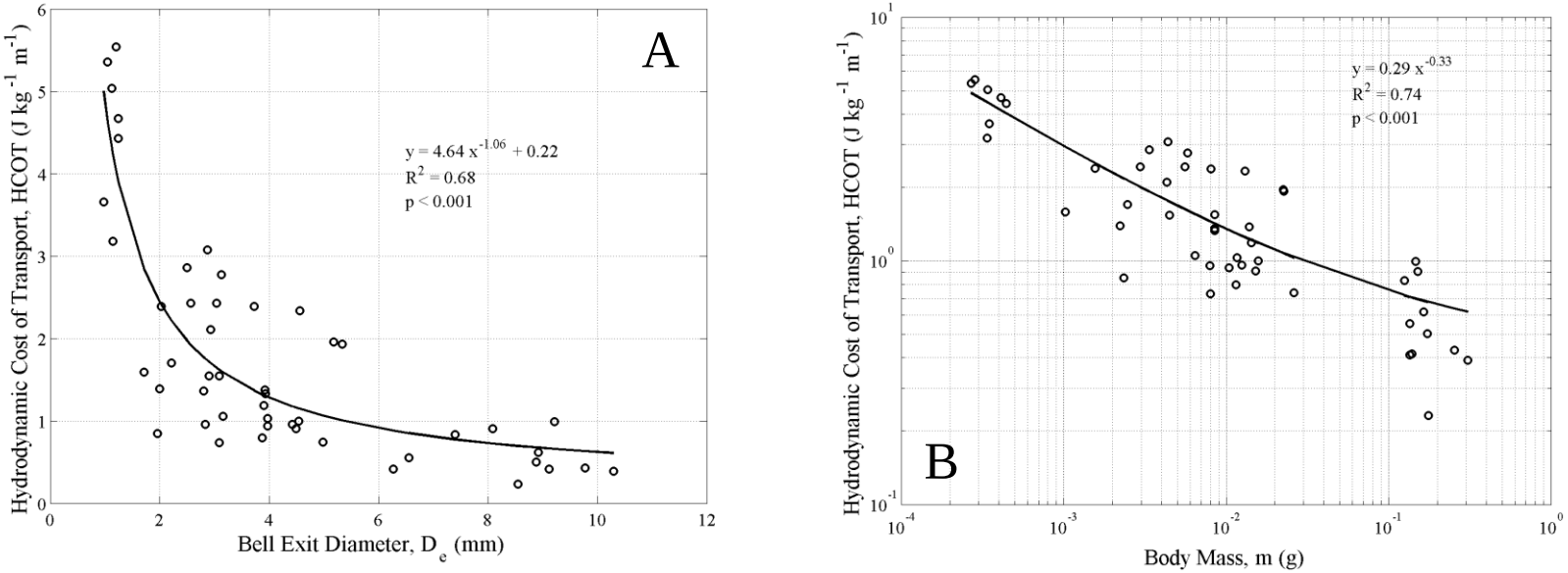

Figure 9